

Cage Structure and Near Room-Temperature Superconductivity in TbH_n ($n = 1-12$)

HPSTAR
1130-2021

Yu-Long Hai, Ning Lu, Hui-Li Tian, Meng-Jing Jiang, Wei Yang, Wen-Jie Li, Xun-Wang Yan, Chao Zhang,* Xiao-Jia Chen,* and Guo-Hua Zhong*



Cite This: *J. Phys. Chem. C* 2021, 125, 3640–3649



Read Online

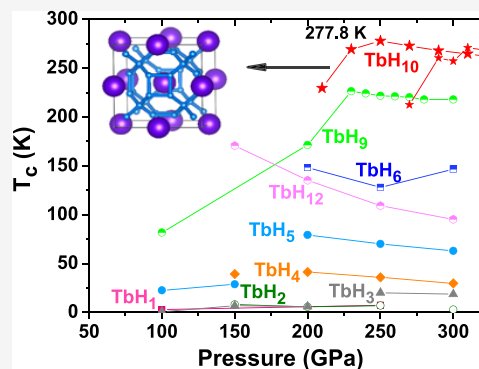
ACCESS |

Metrics & More

Article Recommendations

Supporting Information

ABSTRACT: Hydrogen-rich compounds are considered most likely to achieve room-temperature superconductivity since the critical temperature (T_c) above 250 K was observed in lanthanum hydride. Exploring the high-temperature superconductivity in rare-earth metal hydrides becomes very interesting. Based on the particle swarm optimization for crystal structures and first-principles calculations, we investigate the crystal structures, phase stability, metallization, and possible superconducting properties of terbium hydride (TbH_n , $n = 1-12$) under pressure. Our results show that terbium hydride is a potential high-temperature superconductor under high pressures. It stably exists at different pressure conditions by adjusting the H content. Specifically, the H atomic cage structure can be observed in most terbium hydrides, and the number of H atoms in the cage sublattice increases with the stoichiometry of H in TbH_n . We demonstrate that the high T_c value is closely related to this cage sublattice and it increases with increasing H content in terbium hydride. The highest T_c above 270 K is predicted in TbH_{10} at 250 GPa for $Fm\bar{3}m$ and 310 GPa for $R\bar{3}m$ space group. This result indicates that the superconductivity with T_c close to or beyond lanthanum hydride can be achieved in other rare-earth metal hydrides.



INTRODUCTION

In 2004, Ashcroft suggested that hydrogen-rich compounds can become metallic and superconducting at lower pressures than solid hydrogen,¹ presumably because of “chemical compression” of heavy elements. Hydrogen-rich compound is widely regarded as one of the most promising materials to achieve room-temperature superconductivity. Numerous hydrides have been studied.² From the aspect of the interaction between H and heavy elements, there are two kinds of hydrides respectively containing the polar covalent bond and the ionic bond. The former includes SiH_4 ,^{3,4} H_3S ,^{5,6} PH_3 ,⁷ GeH_4 ,^{8,9} SnH_4 ,¹⁰ PbH_4 ,¹¹ and so on, while the latter is mainly $\text{GeH}_4(\text{H}_2)_2$,¹² $\text{PbH}_4(\text{H}_2)_2$,¹³ CaH_6 ,¹⁴ MgH_6 ,¹⁵ YH_6 ,^{16,17} LaH_{10} ,¹⁸⁻²⁰ etc. In 2015, the discovery of superconductivity in H_3S (critical temperature $T_c \approx 203$ K at 155 GPa⁶) is a milestone in the search of room-temperature superconductors, which means that the superconductivity at more than 200 K was observed in hydrides for the first time. Soon in 2019, the superconductivity near room temperature ($T_c \approx 250$ K at 170 GPa²⁰) was discovered, and the research of high-temperature superconductors has attracted much attention.²¹ From the existing form of H atom in the hydride, the structure of H atoms in hydrides is highly sensitive on superconductivity. Except H_3S , most of the hydrides containing polar covalent bonds exhibit the low T_c such as 75 K of SiH_4 ,⁴ 78 K of PH_2 ,²² 80 K of H_2S ,²³ 45 K of H_2Cl ,²⁴ and 33 K of H_2I .²⁵ The

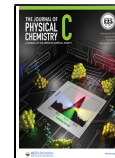
formation of H_2 quasi-molecular units in hydrides results in the increase in T_c , such as 107 K of $\text{SiH}_4(\text{H}_2)_2$,²⁶ $\text{GeH}_4(\text{H}_2)_2$,¹² and $\text{PbH}_4(\text{H}_2)_2$,¹³ indicating that the H “cluster” can drive higher T_c values. The cage configuration of H atoms in CaH_6 ,¹⁴ YH_6 ,¹⁶ and LaH_{10} ¹⁸ supports this idea. The cage sublattice formed by H atoms leads to the T_c near room temperature, even up to 473 K in $\text{Li}_2\text{MgH}_{16}$.²⁷ This kind of cage structure can be viewed as one kind of H cluster. In fact, the distance of H–H in these H cages is similar to that in metallic hydrogen at high pressures.^{15,18}

Compared to alkaline-earth metal hydrides, previous studies have established that rare-earth metal hydrides easily produce the H cage structure. Expect LaH_{10} , the cage character was also observed in other rare-earth metal hydrides such as CeH_9 ,^{28,29} UH_{77} ,³⁰ AcH_{10} ,³¹ ThH_{10} ,^{32,33} PrH_9 ,^{28,35,34} PaH_8 ,³⁶ etc. It was well known that the transition group rare-earth hydrogen-rich compounds have one thing in common. Almost all of these elements contain empty d or f and form what we call the “lability belt”, in which the electronic structure of elements are

Received: January 24, 2021

Revised: January 28, 2021

Published: February 5, 2021



particularly sensitive to the atomic environment because they have empty low-lying orbitals. The population of the orbitals depends on crystal field, making strong electron–phonon coupling possible.³⁵ However, the T_c values of these rare-earth hydrides mentioned above are all lower than that of LaH_{10} . Analyzing the electronic configuration, we know that the difference between La and other rare-earth elements is the absence of the 4f or 5f electrons in La. Then, it is an interesting issue to explore the superconductivity with higher T_c values in 4f or 5f rare-earth metal hydrides under high pressures than the La case.

Terbium is a member of the lanthanide family. The structures of terbium are all close packed and have a high symmetry. At 40.2 and 155 GPa, the phase transition of terbium changes to hR24 and $C2/m$, respectively.³⁷ The increase in pressure directly increases the electron density, which leads to the distortion of the hR24 phase. Upon further compression, the 4f electrons become itinerant. Thus, low symmetry structures can also form at high pressures. This kind of transformation is first-order, which is accompanied by the discontinuous decrease in volume, the decrease in resistivity, and the hardening of lattice. The change of the f-electron behavior under pressure has a significant effect on the superconducting behavior, and f-electron delocalization induces a considerable bond shortening. These effects are observed in rare-earth metals. In addition, the insulator–metal transitions induced by f-electron delocalization are expected in rare-earth monochalcogenides.³⁸ Due to the high-pressure behavior of terbium mentioned above, one is interested in the crystal structure, electronic characteristics, and superconducting properties of terbium hydride ($\text{Tb}-\text{H}$) under high pressures. Can terbium hydride produce better superconductivity than LaH_{10} ? These are all fascinating and open issues. In this work, we examine the electronic structure and bonding of terbium hydride to understand the crystal chemistry of this system and to look for the possible superconductivity with higher temperatures than LaH_{10} by using first-principles calculations.

COMPUTATIONAL DETAILS

Referring to the previous studies on similar hydrogen-rich systems, we know that the crystal structure with one to six formula units (f.u.) in each unit is frequent. Therefore, we searched for possible structures within the framework of about 200 space groups with the CALYPSO code.^{39,40} Due to the different positions of Wyckoff, we consider as many crystal configurations as possible for each space group. Each cell of the candidate structure of $\text{Tb}-\text{H}$ contains one to six f.u. Then, we calculated their total energy and enthalpy at 0, 50, 100, 150, 200, 250, and 300 GPa. The relatively stable structure was selected and extended to other pressure points. All structural optimization was carried out by using the density functional theory of Perdew–Burke–Ernzerhof (PBE) generalized gradient approximation (GGA)⁴¹ and the projector augmented wave pseudopotential⁴² as implemented in the Vienna ab initio simulation package (VASP).^{43,44} The adopted pseudopotentials of Tb and H are from files titled “PAW-PBE Tb 23Dec2003” and “PAW-PBE H 15Jun2001”, respectively. Thus, $4f^35s^25p^66s^2$ of Tb and $1s^1$ of H were treated as valence electrons. $\text{Tb}-\text{H}$ unit cells were sampled from the Brillouin zone (BZ) by the energy cutoff 600 eV plane wave basis. The k -point of the Brillouin zone was a 0.04 \AA^{-1} interval distribution of Monkhorst-Pack for the optimization of

structures, and the k -point interval of the total energy self-consistent calculation was 0.02 \AA^{-1} or better. Convergence thresholds were set as 10^{-5} eV in energy and 10^{-3} eV/ \AA in force.

The QUANTUM ESPRESSO (QE) package^{45,46} was used to examine the dynamical and possible superconducting properties of these compounds. Phonon frequency and electron–phonon coupling (EPC) constant were calculated using density functional perturbation theory,⁴⁷ employing the plane-wave pseudopotential method. The adopted pseudopotentials of Tb and H are from files titled “Tb.pbe-spdn-kjpaw-psl.1.0.0.UPF” and “H.pbe-kjpaw-psl.1.0.0.UPF”, respectively. The $4f^3$ electrons of Tb were treated as valence electrons similar to that in VASP. The cutoff energies were set as 80 and 600 Ry, respectively, which were used for wave function and charge density. The forces and stresses of the converged structure were optimized and controlled within the error range between VASP and QE code.

Considering that Tb is a heavy element, we have tested the spin-orbit coupling (SOC) effect on total energy of the system. In particular, the influence of SOC effect on total energy mainly reflects in the analysis of crystal stability and phase transition. So, we investigated the difference of calculation results with or without SOC correction in the cases of several structures under different pressures. As shown in Figure S1 of the Supporting Information, the SOC correction does not change the phase transition ordering though the pressure point of phase transition has a slight shift. Thus, we conclude that the SOC effect will not essentially change the stability and phase transition ordering of TbH_n under pressure because the SOC is a minor correction in the energy scale. With regard to the electronic correlation effect in TbH_n , we think it is weak under high pressures. It is well known that systems may have different physical properties under high pressures. Pressure is an important physical quantity for hydrides. The 4f electrons become itinerant, and the energy bands near the Fermi level are just broadening under high pressures. Especially, the Hubbard U were calculated by using the linear response approach of Cococcioni et al.⁴⁸ to estimate the strength of electronic correlations. For several typical systems, we obtained $U = 0.74$ eV for TbH_{10} at 250 GPa, $U = 0.96$ eV for TbH_6 at 150 GPa, and $U = 2.3$ eV for TbH_2 at 25 GPa. The results indicate that the electronic correlations in TbH_n are weak at higher pressures such as above 100 GPa. Based on these two tests above, the results will be presented and discussed at the GGA functional level in this work, especially for electronic structures and possible superconductivity of TbH_n at high pressures.

RESULTS AND DISCUSSION

Phase Diagram. Some possible structures of the $\text{Tb}-\text{H}$ system with different H contents have been systematically investigated by using the data package provided by CALYPSO and referring to previous studies.^{14,15,29–36} More than 100 configurations were selected from all the structures with different chemical coordination numbers and low energies. The formation enthalpy of terbium hydride was calculated at 0, 50, 100, 150, 200, 250, and 300 GPa. Also, the formation enthalpy of the $\text{Tb}-\text{H}$ system at different pressures with respect to $\text{Tb} + \text{H}_2$ is shown in the convex hull diagrams of composition–pressure phase diagram (Figure 1). The energetic stability of different terbium hydrides is evaluated by its formation enthalpy. Here, we preferentially explore

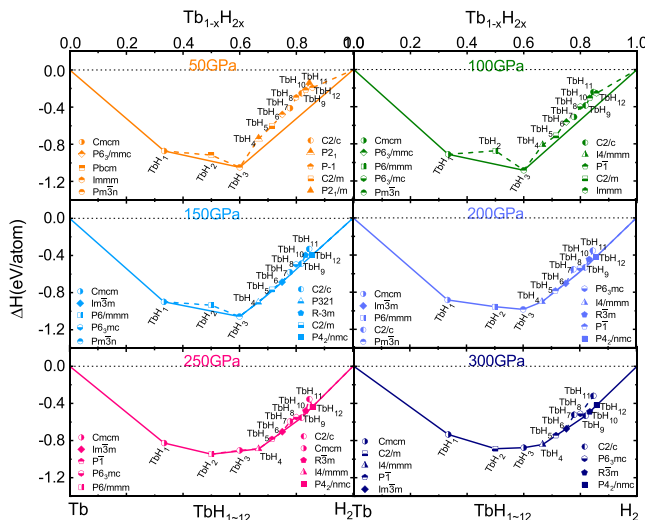


Figure 1. Composition–pressure phase diagram. Phase stability of terbium hydrides with different H contents at selected pressures with respect to $\text{Tb} + \text{H}_2$. The abscissa x is the fraction of H in the structures. Dotted lines (implying the instability) connect the data points, and solid lines denote the convex hull.

terbium hydrides with higher hydrogen contents by compressing the mixture containing Tb and H. For each stoichiometry, up to six formula units are used in the model for calculation at a pressure of 0 – 300 GPa. The basic information can be summarized as follows: (1) At low pressures (0 – 100 GPa), most of the composition compounds are in metastable states, while most of the structures with different stoichiometries are thermodynamically stable above 150 GPa; (2) Notably, only TbH_1 is always stable in the whole pressure range of 0 – 300 GPa, while TbH_7 , TbH_8 , and TbH_{11} are metastable in the whole pressure range considered, which are excluded from later discussion; (3) The higher the ratio of hydrogen to terbium, the lower the formation enthalpy, and the more stable the thermodynamic performance. We will pay more attention to this part of stoichiometry in the later discussion.

Based on the composition–pressure phase diagram above, the stable phases of each TbH_n ($n = 1 – 12$) system are further established. Figure 2 depicts the ordering of phase transition with the increase in pressure for each TbH_n in the pressure range of 0 – 300 GPa. The phase satisfied as the composition–pressure stable relation shown in Figure 1 is defined as the thermodynamically stable phase and plotted by the solid line in Figure 2. On the contrary, the phase dissatisfied as the composition–pressure stable relation shown in Figure 1 is defined as the thermodynamically metastable phase and plotted by the dotted line in Figure 2. It is found that TbH_n with low H contents can be stabilized at low pressures, such as TbH_1 , TbH_2 , and TbH_3 . TbH_1 always has a stable thermodynamical structure with the space group of $Cmcm$ in the whole pressure range of interest. TbH_2 can stably exist below the pressure of 25 GPa with the $Pbcm$ symmetry, and then it is stabilized with the $P6/mmm$ phase from 175 to 275 GPa before transforming to the $C2/m$ phase after 275 GPa. TbH_3 is almost stable in the whole pressure range except for 245 – 255 GPa. At low pressures, TbH_3 stably exists in the form of $Pm\bar{3}n$ symmetry up to 245 GPa, the space group is transformed from $Pm\bar{3}n$ to $Cmcm$ at 245 GPa, and the space group $Cmcm$ is maintained until 300 GPa. As shown in Figure 2, the stable phases of TbH_4 , TbH_5 , TbH_6 , TbH_9 , and TbH_{12}

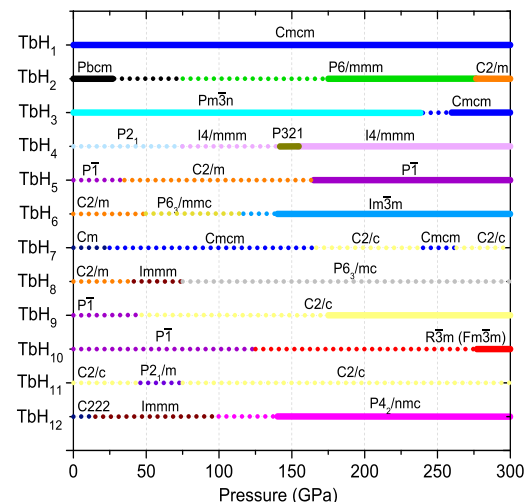


Figure 2. Structure-pressure phase diagram. The stable phases of each TbH_n ($n = 1 - 12$) system dependence on the pressure. The space groups are distinguished by different colored lines. The solid and dotted lines represent the thermodynamically stable and metastable phases, respectively.

appear at the moderate pressures above 125 GPa. For TbH_4 , there are two stable space groups in the pressure ranges of 145 – 155 and 155 – 300 GPa, respectively. The phase transition among stable structures in TbH_4 occurs at about 155 GPa from $P321$ to $I4/mmm$. Meanwhile, the single stable phase exists in TbH_5 ($\bar{P}1$, >160 GPa), TbH_6 ($Im\bar{3}m$, >145 GPa), TbH_9 ($C2/c$, >175 GPa), and TbH_{12} ($P4_2/nmc$, >145 GPa). Interestingly, TbH_{10} is thermodynamically stable in a pressure range of 270 – 300 GPa. The stable space group $\bar{R}\bar{3}m$ is accompanied by a metastable state with the symmetry of $Fm\bar{3}m$. The enthalpy difference between $\bar{R}\bar{3}m$ and $Fm\bar{3}m$ is only 0.06 eV/f.u. They can be considered as two degenerate states of TbH_{10} at high pressures. Considering that $M\text{H}_{10}$ (M = La, Y, Ac, and Th) has achieved exciting results in the previous theoretical prediction and experimental research,^{18–20,31–33} the structure and possible superconductivity in TbH_{10} are also expected in the pressure range of 200 – 350 GPa. Noticeably, some metastable phases (marked by dotted lines) in their corresponding pressure ranges have been also shown in Figure 2 for comparison.

We now examine the above results. Because zero-point energy (ZPE) has been shown to play an important role in determining the stability of hydrogen-rich materials, we consider its effect. We have recomputed the formation enthalpies of different phases in Tb–H at 250 GPa by including ZPE ([Figure S2](#)). As a result, the phases of Tb–H are still stable; therefore, the above conclusions are not altered by considering zero-point vibrations.

Crystal Structures. The crystal structure characteristics of the stable phases for TbH_n at different pressures are shown in Figures 3 and 4. Correspondingly, their crystal unit cells are presented in Figures S3 and S4, and the crystal lattice parameters are summarized in Table S1 of the Supporting Information. It is found that H atoms have difficulty in forming hydrogen clusters in low H content terbium hydrides and at low-pressure conditions. Below 150 GPa, the nearest distance of H–H ($d_{\text{H}-\text{H}}$) in TbH_n is commonly larger than 1.6 Å. From the calculated electron localization functions (ELFs) shown in Figure S5, the bonding interaction among H atoms

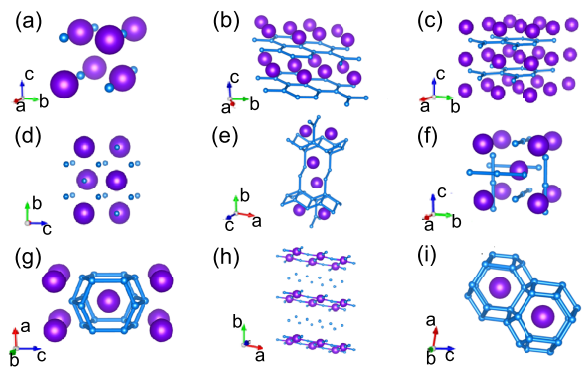


Figure 3. Optimized crystal structures of TbH_n with low H contents. (a) Cmcm phase of TbH_1 at 150 GPa, (b) $\text{C}2/\text{m}$ phase of TbH_2 at 300 GPa, (c) $\text{P}6/\text{mmm}$ phase of TbH_2 at 200 GPa, (d) Pbcm phase of TbH_2 at 20 GPa, (e) Cmcm phase of TbH_3 at 300 GPa, (f) $\text{Pm}3\text{n}$ phase of TbH_3 at 200 GPa, (g) $\text{I}4/\text{mmm}$ phase of TbH_4 at 200 GPa, (h) $\text{P}3\text{2}1$ phase of TbH_4 at 150 GPa, and (i) $\text{P}1$ phase of TbH_5 at 200 GPa. Big and small balls represent Tb and H atoms, respectively.

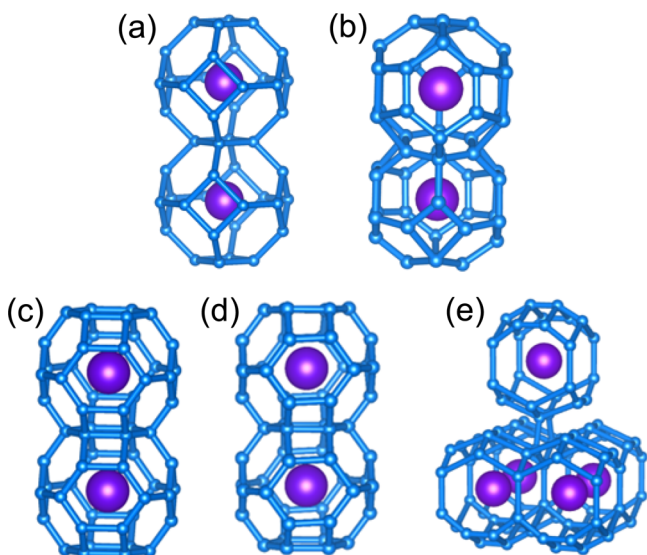


Figure 4. Cage-like feature in optimized crystal structures of TbH_n with high H contents. (a) $\text{Im}3\text{m}$ phase of TbH_6 at 300 GPa, (b) $\text{C}2/\text{c}$ phase of TbH_9 at 300 GPa, (c) $\text{Fm}3\text{m}$ phase of TbH_{10} at 300 GPa, (d) $\text{R}3\text{m}$ phase of TbH_{10} at 300 GPa, and (e) $\text{P}4_2/\text{nmc}$ phase of TbH_{12} at 300 GPa. Big and small balls represent Tb and H atoms, respectively.

lacks in low H content terbium hydrides such as cmcm - TbH_1 (Figure S5a) and at low-pressure conditions such as Pbcm - TbH_2 at 20 GPa (Figure S5d). Above 150 GPa, however, the space among H atoms is compressed with increasing pressure so that H atoms can form the cluster configuration. There are visibly bonding interactions in these high phases as ELF shown in Figures S5 and S6. Moreover, most of the terbium hydride compounds exhibit the cage structures of H atoms similar to CaH_6 and LaH_{10} , such as TbH_4 , TbH_5 , TbH_6 , TbH_9 , TbH_{10} , and TbH_{12} . In these cage structures, the $d_{\text{H}-\text{H}}$ value is often smaller than 1.6 Å, though pressure can drive a small variation of interatomic space. A cage structure consisting of a certain number of hydrogen atoms can interact strongly with the metal atoms in the center within a certain pressure range. Heavy compression makes the distance between the H atom and the central Tb atom, $d_{\text{Tb}-\text{H}}$, short. Thus, the Coulomb

interaction between them is greatly enhanced. At the same time, the distance between the hydrogen atom and the center atom is compressed, which means that the center atom can get more charge. As a result, the electron–phonon interaction is greatly enhanced. Hence, cage structures of the H atoms in hydrides are viewed as the signal of high-temperature superconductivity.

Viewing the structures of terbium hydrides with low H contents, as shown in Figure 3a, we can find that TbH_1 has a very simple crystal structure, just a pair of Tb and H atom and repeating this arrangement in the lattice. In the low-pressure phase Pbcm of TbH_2 shown in Figure 3d, the H atoms can be viewed as the isolated atom without interactions, and the $d_{\text{Tb}-\text{H}}$ value in Pbcm - TbH_2 is 2.19 Å larger than 1.85 Å in Cmcm - TbH_1 . Noticeably, for the high-pressure phases of TbH_2 with the $\text{C}2/\text{m}$ (Figure 3b) and $\text{P}6/\text{mmm}$ (Figure 3c) structures, terbium and hydrogen layers arrange alternately, and H atoms form a graphene-like structure where the $d_{\text{H}-\text{H}}$ value is 1.47 Å at 300 GPa for $\text{C}2/\text{m}$ and 1.60 Å at 200 GPa for the $\text{P}6/\text{mmm}$ phase, respectively. The graphene-like layer structure formed by H atoms is similar to the hydrogen pentagraphene-like structure of HfH_{10} , which is a recently discovered high-temperature superconductor.⁴⁹ In these two high-pressure phases of TbH_2 , H atoms exhibit the strongly bonding interaction as shown in Figures S5b and S5c. For TbH_3 with the Cmcm phase (Figure 3e), terbium and hydrogen atoms arranged alternately in layers, exhibiting the strongly bonding interaction (Figure S5e). For TbH_3 with the $\text{Pm}3\text{n}$ phase (Figure 3f), hydrogen atoms in linear form of H–H–H arrangement on both sides of terbium atoms with the $d_{\text{H}-\text{H}}$ value of about 1.60 Å at 200 GPa, which results in the weak bonding interaction (Figure S5f). Around 150 GPa, as shown in Figure 3h, TbH_4 with the $\text{P}3\text{2}1$ symmetry exhibits the structural characteristics of TbH_1 and TbH_2 . However, as shown in Figure 3g, $\text{I}4/\text{mmm}$ symmetrical TbH_4 forms a cage-like structure of H_{18} with Tb atoms located at the center in the pressure range of 155–300 GPa. The structure of $\text{I}4/\text{mmm}$ - TbH_4 is the same as that of CaH_4 .⁵⁰ The H_{18} cage in $\text{I}4/\text{mmm}$ - TbH_4 consists of four hexagons and eight quadrilaterals in which the average length of H–H bonds is 1.47 Å at a pressure of 200 GPa. As shown in Figure 5, the H–H distance along the c axis becomes bigger while other H–H bonds shorten with

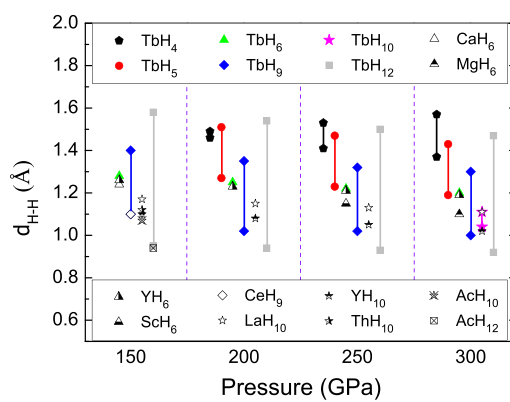


Figure 5. Variation of the nearest H–H distance ($d_{\text{H}-\text{H}}$) in cage-like structures of TbH_n with pressure, comparing with those of CaH_6 ,¹⁴ MgH_6 ,¹⁵ YH_6 ,⁵² ScH_6 ,⁵¹ CeH_9 ,²⁹ LaH_{10} ,¹⁸ YH_{10} ,⁵² ThH_{10} ,³³ AcH_{10} ,³¹ and AcH_{12} .³¹ The bar implies the distribution of the $d_{\text{H}-\text{H}}$ values in the cage configuration.

increasing pressure. Moreover, $P\bar{1}$ symmetrical TbH_5 (Figure 3i) shows a distorted H_{21} cage configuration at high pressures of 160–300 GPa. Differing from $I4/mmm$ - TbH_4 , the H_{21} cage in $P\bar{1}$ - TbH_5 is made up of six quadrilaterals, two pentagons, and five hexagons. The d_{H-H} value varies in the range of 1.27–1.51 Å for the pressure of 200 GPa, and the average value of d_{H-H} decreases with increasing pressure. With the cage characteristics, H atoms exhibit visibly bonding interactions as shown in Figures S5g and S5i. However, as shown in Figure 5, the d_{H-H} value in the H cage structure of TbH_5 is correspondingly larger than those of other rare-earth hydrides at the same pressure.

As mentioned above, the cage feature of H atoms was also observed in TbH_n with high H contents (Figure 4), such as TbH_6 , TbH_9 , TbH_{10} , and TbH_{12} at high pressures. As shown in Figure 4a, the sodalite cage structure in $Im\bar{3}m$ - TbH_6 is similar to that in CaH_6 ¹⁴, MgH_6 ¹⁵, YH_6 ¹⁶, and ScH_6 ⁵¹. The H_{24} cage structure can stably exist in the pressure range of 145–300 GPa, composed of six quadrilaterals and eight hexagons. The H_{24} cage configuration can be also viewed as a result of the interconnection of each H atom on the corner of a quadrilateral with other quadrilaterals, showing the visibly bonding interactions as shown in Figure S6a. Also, two H_{24} cages connect by sharing a quadrilateral in the periodically repeated direction. The d_{H-H} value in the H_{24} cage of $Im\bar{3}m$ - TbH_6 is respectively 1.28, 1.25, 1.22, and 1.20 Å at pressures of 150, 200, 250, and 300 GPa, which is correspondingly larger than 1.24 Å in CaH_6 at 150 GPa¹⁴ and 1.15 Å in ScH_6 at 250 GPa⁵¹ and larger than 1.1 Å in MgH_6 at 300 GPa.¹⁵ The d_{Tb-H} value in $Im\bar{3}m$ - TbH_6 is 2.02 Å at 150 GPa, and then it decreases to 1.90 Å at 300 GPa, which is obviously larger than the d_{Sc-H} value of 1.7 Å in ScH_6 at 200 GPa.

For TbH_9 , the cage structure of the H_{29} cluster can be formed in the $C2/c$ phase and is stable in the pressure range of 175–300 GPa. As shown in Figure 4b, H_{29} is composed of five quadrilaterals, six pentagons, and six hexagons. Differing from H_{24} cages in TbH_6 , two adjacent H_{29} cages in TbH_9 share a hexagon. In the H_{29} cage of $C2/c$ - TbH_9 as shown in Figure 5, the d_{H-H} value varies in a wide range, such as from 1.03 to 1.31 Å at 300 GPa, which implies the difference between H_{24} and H_{29} cages. Taking a pressure of 150 GPa, for example, the d_{H-H} value of 1.1–1.4 Å in $C2/c$ - TbH_9 is larger than 1.1 Å in $P6_3/mmc$ - CeH_9 .²⁹ The d_{Tb-H} value also decreases from 1.93 Å at 200 GPa to 1.80 Å at 300 GPa. It is noted that the average value of d_{H-H} decreases from H_{18} (TbH_4) to H_{21} (TbH_5), through H_{24} (TbH_6) and then to H_{29} (TbH_9) as shown in Figure 5.

As shown in Figures 44dc and , at high pressures above 270 GPa, both stable $R\bar{3}m$ and metastable $Fm\bar{3}m$ phases of TbH_{10} have the similar cage structure of H_{32} , which is composed of 10 hexagons and six quadrilaterals. In the periodical lattice, two adjacent H_{32} cages share a hexagon. At 300 GPa, the d_{H-H} value in the H_{32} cage of the $R\bar{3}m$ phase varies in a small range of 1.04–1.14 Å. Similarly, the d_{H-H} value in the H_{32} cage of the $Fm\bar{3}m$ phase is in the almost same range of 1.03–1.12 Å at 300 GPa, exhibiting strongly bonding characteristics as shown in Figure S6b. Also, it was found that the length of the H–H bond shared by two adjacent hexagons is less than that shared by two adjacent quadrilaterals. In $R\bar{3}m$ - TbH_{10} , the d_{Tb-H} value is about 1.95 Å at 300 GPa, which is larger than 1.80 Å of $C2/c$ - TbH_9 and 1.90 Å of $Im\bar{3}m$ - TbH_6 at the same pressure.

For TbH_{12} with a higher H content, the $P4_2/nmc$ phase is stable at high pressures above 145 GPa and forms a complicated cage-like structure composed of the H_{24} cage as shown in Figure 4e. Five H_{24} cages share a pentagon. Each H_{24} cage contains 12 quadrilaterals and four heptagons, without a hexagon or pentagon. However, the values of d_{H-H} in $P4_2/nmc$ - TbH_{12} possess a wide distribution range at every pressure. In the case of 300 GPa, the d_{H-H} value covers the range from 0.92 to 1.47 Å. At 300 GPa, the d_{Tb-H} value in $P4_2/nmc$ - TbH_{12} is about 1.92 Å, which is slightly smaller than 1.95 Å of $R\bar{3}m$ - TbH_{10} . Especially, this kind of coupling among H_{24} cages and the smaller distance of d_{Tb-H} read to the better stability in TbH_{12} , so it can exit at lower pressures than TbH_{10} .

The higher the hydrogen content, the easier the formation of the cage structure of H atoms, and the larger the cage size. Moreover, examining the d_{H-H} data of TbH_n shown in Figure 5, we find that the nearest distance of H–H in TbH_4 , TbH_6 , and TbH_{10} has a smaller oscillation than that of TbH_5 , TbH_9 , and TbH_{12} . This is possibly due to the presence of pentagons (or heptagons) unit or the existence of more than two kinds of hydrogen units in TbH_5 , TbH_9 , and TbH_{12} . For example, there are only quadrilaterals and hexagons in TbH_4 , TbH_6 , and TbH_{10} . However, by comparison, the d_{H-H} value in terbium hydrides with the H cage structure is larger than those of other rare-earth hydrides and metal hydrides containing the H cage structure in general. In addition, the d_{Tb-H} value is often smaller than 2 Å at high pressures above 150 GPa.

Metallization and Electronic Characteristics. As a traditional superconductor, metallization is a necessary condition to superconduct. Before estimating whether terbium hydride is a superconductor, we have investigated the electronic structures of TbH_n ($n = 1$ –12). The electronic total density of states (DOS) and band structures were calculated and are presented in Figures S7–S24. It is found that the thermodynamically stable TbH_n exhibits the metallic behavior in electronic characteristics and energy band structures in the corresponding stable pressure range, even at ambient pressure for TbH_1 and TbH_2 with low stoichiometric ratios of H. Considering that GGA usually underestimates the energy band gap, we also check the electronic structures with the more accurate hybrid functional method (HSE06)⁵³ in the case of TbH_{10} shown in Figure S25. Comparing Figure S21 and Figure S25, the result shows that no obvious change occurs in DOSs of TbH_{10} within the framework of HSE06, especially for the DOS value at the Fermi level. This indicates that the metallization based on the GGA level is reliable. Two or more energy bands cross the Fermi level in each stable phase of terbium hydride, forming the complicated Fermi surface morphology composed of electron-like and hole-like sheets. To investigate the fine characteristics of electronic states, we have presented the total DOS and the projected density of states (PDOS) on atoms and orbitals of several typical cases including different pressures and different stoichiometries in Figure 6. It is found that the state feature of Tb-4f is very prominent. The electronic states near the Fermi level are mainly from Tb-4f, while the electronic states of H are scanty, especially for low-pressure situation. The composition of electronic states near the Fermi level in TbH_n is obviously different from other metal hydrides such as $GeH_4(H_2)_2$,¹² $PbH_4(H_2)_2$,¹³ MgH_6 ,¹⁵ YH_6 ,¹⁶ and LaH_{10} ,¹⁸ in which the electronic states of the H element are almost comparable with metals in the order of magnitude. Thus, the complicated Fermi surface of TbH_n is just induced by the

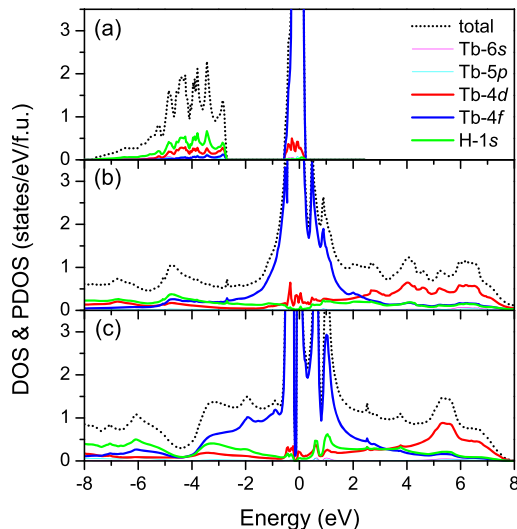


Figure 6. Calculated DOS and PDOS of terbium hydride. Zero energy denotes the Fermi level. (a) $Pbcm$ -TbH₂ at 25 GPa, (b) $Im\bar{3}m$ -TbH₆ at 150 GPa, and (c) $R\bar{3}m$ -TbH₁₀ at 310 GPa.

polymorphic Tb-4f orbital. Of course, slightly away from the Fermi level, the contribution of H to total electronic states is comparable with Tb, as shown in Figure 6.

Furthermore, Figure 6 indicates that the local characteristics of 4f electrons is obvious in TbH_n with low H stoichiometries under low pressures, but 4f electronic states are delocalized under high pressures, which further indicates that the electronic correlation effect in TbH_n is strong at low pressures while it is weak at high pressures. The broadening of the 4f electronic states with increasing pressure shown in Figure 6 results from the enhancement of hybridization interaction between s and f electrons in TbH_n upon compression. From the crystal structure shown in Figure S26, the coordination of Tb in TbH_n is increased with the increase in pressure and components. The charge transfer reduces from 1.3e in TbH₂ at 25 GPa to 0.8e in TbH₁₀ at 310 GPa. The Tb–H bond length shortens from 2.19 Å in TbH₂ at 25 GPa to 1.93 Å in TbH₁₀ at 310 GPa. From the calculated ELF s at different pressures shown in Figure S27, the hybridization interaction between Tb and H also been shown to be enhanced with the increase in pressure. These are reasons that the electron correlation of TbH_n decreases under pressure. In a word, pressure is an important physical quantity for hydrides. For the high-pressure phases of TbH_n, the 4f electron correlations are relatively weak. So, for the following discussion of superconductivity, we will focus on the high-pressure phase of TbH_n.

Dynamical Properties and Superconductivity. For thermodynamically stable Tb–H phases, the calculated phonon spectra shown in Figures S28–S39 also confirm their dynamical stability because there is no imaginary frequency. Then, based on the obtained phonon frequency, we tried to analyze the possible superconductivity for high phases (≥ 100 GPa) of the Tb–H system by calculating the EPC constant (λ), the logarithmic average of phonon frequency (ω_{\log}), and the T_c . In this work, the λ is defined by integration over the entire frequency domain of the Eliashberg electron–phonon spectral function [$\alpha^2 F(\omega)$], where ω represents the phonon frequency, expressed as

$$\lambda = 2 \int_0^\infty \frac{\alpha^2 F(\omega)}{\omega} d\omega \quad (1)$$

The ω_{\log} is written as

$$\omega_{\log} = \exp \left[\frac{2}{\lambda} \int_0^\infty \frac{\alpha^2 F(\omega) \log(\omega)}{\omega} d\omega \right] \quad (2)$$

The T_c is presented by the Allen–Dynes-corrected McMillan equation⁵⁴

$$T_c = f_1 f_2 \frac{\omega_{\log}}{1.2} \exp \left[-\frac{1.04(1 + \lambda)}{\lambda - \mu^*(1 + 0.62\lambda)} \right] \quad (3)$$

Here, μ^* in eq 3 is the Coulomb pseudopotential representing the Coulomb repulsion. The typical value of μ^* is in the range of 0.1–0.13 for hydrides. The factor $f_1 f_2$ is decided by the λ , μ^* , ω_{\log} , and mean square frequency (ω_2).⁵⁴ Table 1 summarizes the calculated superconducting parameters of stable TbH_n in the form of different phases at high pressures.

From the results listed in Table 1, we can claim that terbium hydride is superconducting under high pressures. In general, the electron–phonon interaction and T_c obviously depend on the H content in TbH_n. Weak or moderate strength EPCs were obtained in TbH_n with low H contents, while a strong EPC of $\lambda > 1.5$ could be driven in TbH_n with high H contents such as $n \geq 6$. At the same time, T_c increases with the increase in H content and reaches the highest value in TbH₁₀, and then it has a slight drop in TbH₁₂. For every TbH_n, the relation between T_c and pressure is not monotonous. Especially, the graphene-like layer structures formed by H atoms in TbH₂ with $C\bar{2}/m$ and $P\bar{6}/mmm$ phases did not have the high T_c values similar to HfH₁₀.⁴⁹ However, the cage structure of H atoms obviously leads to higher superconducting critical temperatures, which is consistent with perspectives of Zurek et al.⁵⁵ In the moderate pressure range of 100–200 GPa, the electron–phonon interaction is considerable such as $\lambda = 0.57$ for $P\bar{6}/mmm$ -TbH₂ at 150 GPa, $\lambda = 0.84$ for $Pm\bar{3}n$ -TbH₃ at 150 GPa, $\lambda = 0.72$ for $P\bar{3}21$ -TbH₄ at 150 GPa, and $\lambda = 1.95$ for $P4_2/nmc$ -TbH₁₂ at 150 GPa. As a result, the T_c can highly reach to 170.5 K in $P4_2/nmc$ -TbH₁₂ at 150 GPa, indicating that terbium hydride is a promising high-temperature superconducting material. In the higher pressure region above 200 GPa, with help of the stronger EPC of $\lambda > 1.5$, the superconductivity with a T_c beyond 270 K can be achieved in TbH₁₀ with $Fm\bar{3}m$ and $R\bar{3}m$ symmetries at 250 and 310 GPa, respectively. This T_c value in TbH₁₀ has caught up with that in LaH₁₀, close to room temperature. Significantly, this is the highest value ever reported in rare-earth metal hydrides containing f electrons.

Focusing on terbium hydride containing the H cage, as shown in Table 1, we found that the maximum T_c is proportional to the number of atoms in the H cage. The H₁₈ cage in $I4/mmm$ -TbH₄ can produce $T_c \approx 41.3$ K at 200 GPa, and the H₂₁ cage in $P\bar{1}$ -TbH₅ can push T_c to 79.3 K at 200 GPa; furthermore, the H₂₄ cage in $Im\bar{3}m$ -TbH₆ drives a higher $T_c \approx 148.3$ K at 200 GPa, while H₂₉ and H₃₂ cages in TbH₉ and TbH₁₀ respectively create superconductivity with a T_c far beyond 200 K. TbH₁₂ is a special case in which H atoms form three interconnected H₂₄ cages so that the T_c of TbH₁₂ is similar to that of TbH₆ at the same pressure. On one hand, as shown in Figure 5, the nearest d_{H-H} slightly decreases with increasing size of the cage, yielding the highest phonon

Table 1. Calculated EPC Constant λ , Logarithmic Average of Phonon Frequency ω_{\log} , and Critical Temperature T_c for Stable TbH_n

TbH_n	space group	pressure (GPa)	λ	ω_{\log} (K)	T_c (K)	
					$\mu^* = 0.10$	$\mu^* = 0.13$
TbH_1	$Cmcm$	100	0.50	232.4	2.9	1.8
	$Cmcm$	250	0.62	284.2	7.3	5.2
TbH_2	$P\bar{6}/mmm$	150	0.57	405.8	8.06	5.45
	$P\bar{6}/mmm$	200	0.60	238.5	5.64	3.96
TbH_3	$P\bar{6}/mmm$	250	0.52	479.5	7.01	4.40
	$C2/m$	300	0.42	520.8	2.78	1.30
TbH_4	$Pm\bar{3}n$	100	0.34	489.9	0.74	0.21
	$Pm\bar{3}n$	150	0.84	125.3	6.81	5.57
TbH_5	$Pm\bar{3}n$	200	1.14	65.9	6.01	5.28
	$Cmcm$	250	0.63	718.5	20.0	14.5
TbH_6	$Cmcm$	300	0.60	781.1	18.7	13.1
	$P321$	150	0.72	987.2	39.3	30.4
TbH_7	$I4/mmm$	200	0.70	1143.5	41.3	31.3
	$I4/mmm$	250	0.65	1188.8	35.9	26.3
TbH_8	$I4/mmm$	300	0.60	1222.1	29.7	21.0
	$P\bar{1}$	200	0.98	1067.5	79.3	67.1
TbH_9	$P\bar{1}$	250	0.89	1129.3	70.1	57.9
	$P\bar{1}$	300	0.82	1184.2	62.8	50.8
TbH_{10}	$Im\bar{3}m$	200	1.58	1028.3	148.3	132.6
	$Im\bar{3}m$	250	1.55	905.9	127.9	114.6
TbH_{11}	$Im\bar{3}m$	300	1.48	1094.9	146.6	130.1
	$C2/c$	200	3.08	604.4	171.4	163.2
TbH_{12}	$C2/c$	230	2.08	1191.4	226.3	204.7
	$C2/c$	240	1.97	1252.8	224.2	202.9
TbH_{13}	$C2/c$	250	1.87	1311.7	221.6	200.4
	$C2/c$	260	1.80	1360.4	221.1	199.8
TbH_{14}	$C2/c$	280	1.69	1438.5	217.9	196.5
	$C2/c$	300	2.00	1219.9	217.9	203.4
TbH_{15}	$R\bar{3}m$	270	2.86	777.9	212.5	191.8
	$R\bar{3}m$	290	2.34	1255.4	260.4	245.2
TbH_{16}	$R\bar{3}m$	310	2.13	1395.6	270.9	245.4
	$R\bar{3}m$	330	1.98	1487.6	266.5	241.4
TbH_{17}	$R\bar{3}m$	350	1.85	1571.2	262.5	237.5
	$Fm\bar{3}m$	210	4.20	603.6	229.5	220.3
TbH_{18}	$Fm\bar{3}m$	230	3.06	996.4	269.1	256.1
	$Fm\bar{3}m$	250	2.50	1225.1	277.8	252.3
TbH_{19}	$Fm\bar{3}m$	270	2.25	1341.8	272.7	247.9
	$Fm\bar{3}m$	290	2.07	1433.8	267.8	243.3
TbH_{20}	$Fm\bar{3}m$	310	1.95	1512.1	264.7	240.2
	$Fm\bar{3}m$	330	1.84	1579.8	260.5	236.1
TbH_{21}	$Fm\bar{3}m$	350	1.74	1642.5	255.8	231.3
	$P4_2/nmc$	150	1.95	980.2	170.5	158.9
TbH_{22}	$P4_2/nmc$	200	1.17	1396.8	135.3	117.9
	$P4_2/nmc$	250	0.96	1548.9	109.1	91.8
	$P4_2/nmc$	300	0.86	1645.3	95.2	77.9

frequency induced by H–H vibrations shift in a high level. However, on the other hand, as shown in Figures 3 and 4, from TbH_4 to TbH_{10} , the increase in number of atoms in H cages increases the size of cages. This leads to the decrease in distance among H atoms so that the phonon vibrations among H atoms become weak. This means that, at the same pressure, the phonon dispersion will spread toward the low-frequency region (see Figures S33–S38), such as the lowest phonon frequency of H atoms from $\sim 1090 \text{ cm}^{-1}$ of $I4/mmm$ - TbH_4 at 250 GPa to $\sim 510 \text{ cm}^{-1}$ of $R\bar{3}m$ - TbH_{10} at 250 GPa. As a result,

the moderate phonon frequencies become softer with increasing number of atoms in H cages. From the EPC integral $\lambda(\omega)$, the soft modes of phonon mainly contribute to the EPC. Hence, the H cage structure results in the stronger EPC and higher T_c value in terbium hydride, and the T_c will be higher with the increase in the number of atoms in the H cage.

The highest T_c value of terbium hydride was predicted in TbH_{10} . As mentioned above, TbH_{10} stably exists in two forms of $R\bar{3}m$ and $Fm\bar{3}m$ phases at the pressure of ≥ 270 GPa. $R\bar{3}m$ and $Fm\bar{3}m$ phases can be viewed as degenerate states of TbH_{10} in energy. Interestingly, the $Fm\bar{3}m$ phase is dynamically stable in the relatively low-pressure range of $210 – 270$ GPa, though its thermodynamical stability is a little worse in this pressure range. Therefore, the investigation of superconductivity of TbH_{10} has been extended to a larger pressure range. As shown in Table 1, in the pressure range of $270 – 350$ GPa, the $R\bar{3}m$ phase exhibits the superconductivity with $T_c > 200$ K. So, the $Fm\bar{3}m$ phase does in the pressure range of $210 – 350$ GPa. For both $R\bar{3}m$ and $Fm\bar{3}m$ phases, the change of T_c with pressure displays a maximum value, namely, 270.9 K at 310 GPa for the $R\bar{3}m$ phase and 277.8 K at 250 GPa for the $Fm\bar{3}m$ phase. For this best superconductivity, the λ value reaches to 2.13 for $R\bar{3}m$ and 2.50 for the $Fm\bar{3}m$ phase, and the ω_{\log} value is about 1395.6 K for $R\bar{3}m$ and 1225.1 K for the $Fm\bar{3}m$ phase, respectively, meaning that a very strong EPC is formed in TbH_{10} . Figures 7 and 8 show the phonon spectra, phonon

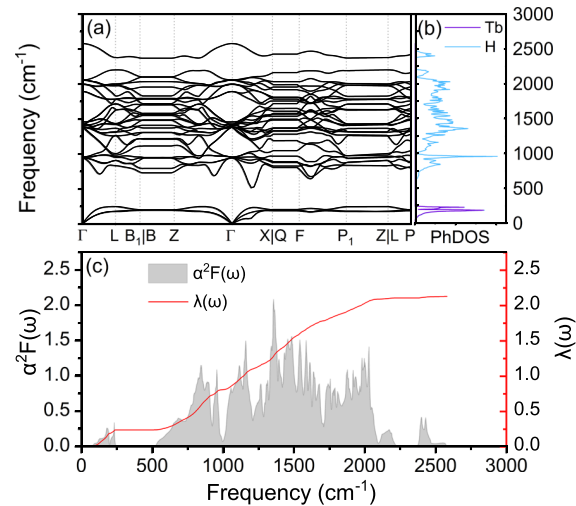


Figure 7. Calculated phonon spectra, phonon density of states (PhDOS), Eliashberg spectral function $\alpha^2F(\omega)$, and electron–phonon coupling integral $\lambda(\omega)$ of $R\bar{3}m$ - TbH_{10} at 310 GPa.

density of states (PhDOS), Eliashberg spectral function $\alpha^2F(\omega)$, and EPC integral $\lambda(\omega)$ of $R\bar{3}m$ and $Fm\bar{3}m$ phases at pressures of 310 and 250 GPa, respectively. For the $R\bar{3}m$ phase at 310 GPa, the phonon bands (Figures 7a and b) are visibly divided into two parts of $0 – 250$ and $520 – 2578 \text{ cm}^{-1}$. The low-frequency region is completely from the Tb vibrations, while the high phonon frequencies above 520 cm^{-1} are mainly contributed by H vibrations. From the Eliashberg spectral function shown in Figure 7c, we can find that the contribution of Tb to total EPC is only 11%, while the H cage contributes about 89% to the total EPC. In terbium hydride, the Tb element mainly provides charge to H atoms, which is the main reason for metallization. Combining the absence of electronic states of H atoms at the Fermi level as shown in Figure 6, we

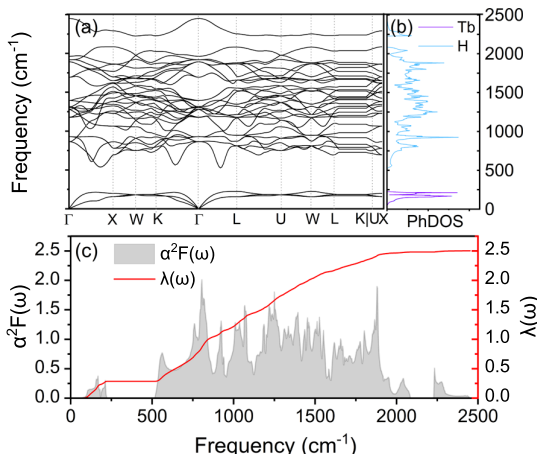


Figure 8. Calculated phonon spectra, phonon density of states (PhDOS), Eliashberg spectral function $\alpha^2 F(\omega)$, and electron–phonon coupling integral $\lambda(\omega)$ of $Fm\bar{3}m$ - TbH_{10} at 250 GPa.

can identify that the contribution of Tb is to the electron aspect while the contribution of H is to the phonon aspect during the EPC process. Namely, the superconductivity of terbium hydride can be visually viewed as the motion of Tb-4f electrons in the lattice field formed by H atoms. The phonon structures and the EPC of the $Fm\bar{3}m$ phase at 250 GPa shown in Figure 8 are similar to those of the $R\bar{3}m$ phase at 310 GPa. The H cage also contributes about 89% to the total EPC.

Remarkably, when the pressure drops to 230 GPa, the T_c of the $Fm\bar{3}m$ phase is still around 270 K. From Table 1, the superconductivity with a T_c above 250 K covers a wide pressure range, such as from 230 to 350 GPa for the $Fm\bar{3}m$ phase and from 290 to 350 GPa for the $R\bar{3}m$ phase. In addition, TbH_9 also exhibits the high-temperature superconductivity of above 200 K in the pressure range of 230 – 300 GPa. Moreover, both TbH_{12} and TbH_6 have the superconductivity with a T_c beyond 100 K in a wide pressure range as shown in Table 1. These results show that the high-temperature superconductivity of terbium hydride is very solid and interesting. Reviewing the superconductivity of terbium hydride, we find that the highest T_c value is almost equal to 274 K of LaH_{10} at 250 GPa, though it is less than 326 K of YH_{10} .¹⁸ Especially, in rare-earth metal hydrides containing f electrons, the $T_c \approx 278$ K in TbH_{10} is remarkable, such as typically higher than 117 K of CeH_9 ,²⁹ 251 K of AcH_{10} ,³¹ and 221 K of ThH_{10} .³² The coupling between Tb-4f electrons and H phonons plays a key role since the higher f electronic density of states is obtained at the Fermi level in terbium hydride. However, as far as we know, there are no reports about the experimental synthesis of terbium hydrides. The superconductivity of terbium hydrides still needs further experimental verification. We are also trying the experimental synthesis of this hydride. More experimental and theoretical investigations will be presented in the future.

CONCLUSIONS

In summary, we have systematically studied the crystal structures, thermodynamical stability, electronic states, dynamical properties, and electron–phonon interactions of binary terbium hydride TbH_n ($n = 1 – 12$). The results successfully revealed the structure and superconductivity of the binary terbium hydride under pressure. We predicted the highest $T_c \approx$

278 K in terbium hydride. Our findings can be summarized as follows:

- (1) All of TbH_7 , TbH_8 , and TbH_{11} are unable to be stable in our considered pressure range. Three stoichiometric compounds of TbH_1 , TbH_2 , and TbH_3 with low H contents have both high-pressure and low-pressure stable phases, while terbium hydride of other chemical proportions is only stable at high pressures above 150 GPa. Interestingly, the cage configuration was observed in high phases of TbH_4 , TbH_5 , TbH_6 , TbH_9 , TbH_{10} , and TbH_{12} , in which the cage size increases with the increase in H content in TbH_n .
- (2) TbH_n exhibits the metallic characteristics under pressure, and the metallization comes from the double effects of charge transfer and pressure. Tb-4f electrons mainly contribute to the states at the Fermi level.
- (3) The thermodynamically stable TbH_n is almost dynamically stable. The phonon bands of TbH_n are obviously divided into two parts, with Tb phonon modes in the low-frequency region and H phonon modes in the high-frequency region. With the increase in H content in TbH_n , especially with the increase in the H cage size, the phonon dispersion broadens and more and more softening modes are formed. Thus, the T_c increases with increasing the H content in TbH_n , especially with the increase in the H cage size. $I4/mmm$ - TbH_4 exhibits the superconductivity with $T_c \approx 40$ K at 200 GPa. $P\bar{1}$ - TbH_5 has $T_c \approx 80$ K at 200 GPa. Meanwhile, in $I\bar{m}\bar{3}m$ - TbH_6 , the T_c was predicted as ~ 150 K at 200 GPa. Furthermore, the T_c around 220 K was presented in $C2/c$ - TbH_9 in the pressure range of 230 – 300 GPa. Excitedly, TbH_{10} with $R\bar{3}m$ and $Fm\bar{3}m$ symmetries both possess the near room-temperature superconductivity of $T_c \approx 270$ K, respectively, above 270 and 230 GPa. TbH_{12} exhibits the similar superconductivity to TbH_6 at the same pressure. The superconductivity of terbium hydride is suggested to be due to the motion of Tb-4f electrons in the lattice field formed by H atoms.

Finally, this study indicates that the superconductivity close to or beyond lanthanum hydride can be achieved in rare-earth metal hydrides TbH_n .

ASSOCIATED CONTENT

Supporting Information

The Supporting Information is available free of charge at <https://pubs.acs.org/doi/10.1021/acs.jpcc.1c00645>.

The crystal structures of TbH_n , the crystal lattice parameters of TbH_n , the electronic structures of TbH_n , the zero-point energy effect, the phonon spectra, and superconducting parameters of TbH_n (PDF)

AUTHOR INFORMATION

Corresponding Authors

Chao Zhang – School of Opto-electronic Information Science and Technology, Yantai University, Yantai 264005, China; orcid.org/0000-0002-5957-2287; Email: phyczhang@ytu.edu.cn

Xiao-Jia Chen – School of Science, Harbin Institute of Technology, Shenzhen 518055, China; Center for High Pressure Science and Technology Advanced Research, Shanghai 201203, China; orcid.org/0000-0003-3921-9424; Email: xjchen@hpstar.ac.cn

Guo-Hua Zhong — Shenzhen Institutes of Advanced Technology, Chinese Academy of Sciences, Shenzhen 518055, China; University of Chinese Academy of Sciences, Beijing 100049, China;  orcid.org/0000-0003-0673-8738; Phone: +86 755 86392129; Email: gh.zhong@siat.ac.cn; Fax: +86 755 86392299

Authors

Yu-Long Hai — Shenzhen Institutes of Advanced Technology, Chinese Academy of Sciences, Shenzhen 518055, China; Nano Science and Technology Institute, University of Science and Technology of China, Suzhou 215123, China

Ning Lu — Shenzhen Institutes of Advanced Technology, Chinese Academy of Sciences, Shenzhen 518055, China; Nano Science and Technology Institute, University of Science and Technology of China, Suzhou 215123, China

Hui-Li Tian — Shenzhen Institutes of Advanced Technology, Chinese Academy of Sciences, Shenzhen 518055, China; Nano Science and Technology Institute, University of Science and Technology of China, Suzhou 215123, China

Meng-Jing Jiang — Shenzhen Institutes of Advanced Technology, Chinese Academy of Sciences, Shenzhen 518055, China; Nano Science and Technology Institute, University of Science and Technology of China, Suzhou 215123, China

Wei Yang — Shenzhen Institutes of Advanced Technology, Chinese Academy of Sciences, Shenzhen 518055, China; Nano Science and Technology Institute, University of Science and Technology of China, Suzhou 215123, China

Wen-Jie Li — Shenzhen Institutes of Advanced Technology, Chinese Academy of Sciences, Shenzhen 518055, China; University of Chinese Academy of Sciences, Beijing 100049, China

Xun-Wang Yan — College of Physics and Engineering, Qufu Normal University, Qufu, Shandong 273165, China;  orcid.org/0000-0001-8108-0791

Complete contact information is available at:

<https://pubs.acs.org/10.1021/acs.jpcc.1c00645>

Notes

The authors declare no competing financial interest.

ACKNOWLEDGMENTS

The work was supported by the Basic Research Program of Shenzhen (grant nos. JCYJ20180507182445460 and JCYJ20200109112810241), the National Natural Science Foundation of China (grant nos. 12074401, 11874318, and 11974207), and the Natural Science Foundation of Shandong Province (grant no. ZR2018MA043). The calculations were performed in the HPC Lab, National Supercomputing Center in Shenzhen and the Beijing Computational Science Research Center.

REFERENCES

- (1) Ashcroft, N. W. Hydrogen Dominant Metallic Alloys: High Temperature Superconductors? *Phys. Rev. Lett.* **2004**, *92*, 187002.
- (2) Mao, H.-K.; Chen, X.-J.; Ding, Y.; Li, B.; Wang, L. Solids, Liquids, and Gases under High Pressure. *Rev. Mod. Phys.* **2018**, *90*, No. 015007.
- (3) Chen, X.-J.; Struzhkin, V. V.; Song, Y.; Goncharov, A. F.; Ahart, M.; Liu, Z.; Mao, H.-K.; Hemley, R. J. Pressure-Induced Metallization of Silane. *Proc. Natl. Acad. Sci. U. S. A.* **2008**, *105*, 20–23.
- (4) Chen, X.-J.; Wang, J.-L.; Struzhkin, V. V.; Mao, H.-K.; Hemley, R. J.; Lin, H.-Q. Superconducting Behavior in Compressed Solid SiH₄ with a Layered Structure. *Phys. Rev. Lett.* **2008**, *101*, 077002.
- (5) Duan, D.; Liu, Y.; Tian, F.; Li, D.; Huang, X.; Zhao, Z.; Yu, H.; Liu, B.; Tian, W.; Cui, T. Pressure-Induced Metallization of Dense (H₂S)₂H₂ with High-T_c Superconductivity. *Sci. Rep.* **2014**, *4*, 6968.
- (6) Drozdov, A. P.; Eremets, M. I.; Troyan, I. A.; Ksenofontov, V.; Shylin, S. I. Conventional Superconductivity at 203 Kelvin at High Pressures in the Sulfur Hydride System. *Nature* **2015**, *525*, 73–76.
- (7) Liu, H.; Li, Y.; Gao, G.; Tse, J. S.; Naumov, I. I. Crystal Structure and Superconductivity of PH₃ at High Pressures. *J. Phys. Chem. C* **2016**, *120*, 3458–3461.
- (8) Gao, G.; Oganov, A. R.; Bergara, A.; Martinez-Canales, M.; Cui, T.; Iitaka, T.; Ma, Y.; Zou, G. Superconducting High Pressure Phase of Germane. *Phys. Rev. Lett.* **2008**, *101*, 107002.
- (9) Zhang, C.; Chen, X.-J.; Li, Y.-L.; Struzhkin, V. V.; Hemley, R. J.; Mao, H.-K.; Zhang, R.-Q.; Lin, H.-Q. Superconductivity in Hydrogen-Rich Material: GeH₄. *J. Supercond. Novel Magn.* **2010**, *23*, 717–719.
- (10) Tse, J. S.; Yao, Y.; Tanaka, K. Novel Superconductivity in Metallic SnH₄ under High Pressure. *Phys. Rev. Lett.* **2007**, *98*, 117004.
- (11) Zaleski-Ejgierd, P.; Hoffmann, R.; Ashcroft, N. W. High Pressure Stabilization and Emergent forms of PbH₄. *Phys. Rev. Lett.* **2011**, *107*, No. 037002.
- (12) Zhong, G.; Zhang, C.; Chen, X.; Li, Y.; Zhang, R.; Lin, H. Structural, Electronic, Dynamical, and Superconducting Properties in Dense GeH₄(H₂)₂. *J. Phys. Chem. C* **2012**, *116*, 5225–5234.
- (13) Cheng, Y.; Zhang, C.; Wang, T.; Zhong, G.; Yang, C.; Chen, X.-J.; Lin, H.-Q. Pressure-Induced Superconductivity in H₂-Containing Hydride PbH₄(H₂)₂. *Sci. Rep.* **2015**, *5*, 16475.
- (14) Wang, H.; Tse, J. S.; Tanaka, K.; Iitaka, T.; Ma, Y. Superconductive Sodalite-Like Clathrate Calcium Hydride at High Pressures. *Proc. Natl. Acad. Sci. U. S. A.* **2012**, *109*, 6463–6466.
- (15) Feng, X.; Zhang, J.; Gao, G.; Liu, H.; Wang, H. Compressed Sodalite-Like MgH₆ as a Potential High-Temperature Superconductor. *RSC Adv.* **2015**, *5*, 59292.
- (16) Li, Y.; Hao, J.; Liu, H.; Tse, J. S.; Wang, Y.; Ma, Y. Pressure-Stabilized Superconductive Yttrium Hydrides. *Sci. Rep.* **2015**, *5*, 9948.
- (17) Troyan, I. A.; Semenok, D. V.; Kvashnin, A. G.; Ivanova, A. G.; Prakapenka, V. B.; Greenberg, E.; Gavriliuk, A. G.; Lyubutin, I. S.; Struzhkin, V. V.; Oganov, A. R. Synthesis and Superconductivity of Yttrium Hexahydride $\text{Im}\bar{3}m\text{-YH}_6$. arXiv:1908.01534, 2019, <https://arxiv.org/abs/1908.01534>.
- (18) Liu, H.; Naumov, I. I.; Hoffmann, R.; Ashcroft, N. W.; Hemley, R. J. Potential High-T_c Superconducting Lanthanum and Yttrium Hydrides at High Pressure. *Proc. Natl. Acad. Sci. U. S. A.* **2017**, *114*, 6990–6995.
- (19) Somayazulu, M.; Ahart, M.; Mishra, A. K.; Geballe, Z. M.; Baldini, M.; Meng, Y.; Struzhkin, V. V.; Hemley, R. J. Evidence for Superconductivity above 260 K in Lanthanum Superhydride at Megabar Pressures. *Phys. Rev. Lett.* **2019**, *122*, No. 027001.
- (20) Drozdov, A. P.; Kong, P. P.; Minkov, V. S.; Besedin, S. P.; Kuzovnikov, M. A.; Mozaffari, S.; Balicas, L.; Balakirev, F. F.; Graf, D. E.; Prakapenka, V. B.; et al. Superconductivity at 250 K in Lanthanum Hydride under High Pressures. *Nature* **2019**, *569*, 528–531.
- (21) Struzhkin, V.; Li, B.; Ji, C.; Chen, X.-J.; Prakapenka, V.; Greenberg, E.; Troyan, I.; Gavriliuk, A.; Mao, H.-K. Superconductivity in La and Y Hydrides: Remaining Questions to Experiment and Theory. *Matter Radiat. Extremes* **2020**, *5*, No. 028201.
- (22) Shamp, A.; Terpstra, T.; Bi, T.; Falls, Z.; Avery, P.; Zurek, E. Decomposition Products of Phosphine under Pressure: PH₂ Stable and Superconducting? *J. Am. Chem. Soc.* **2016**, *138*, 1884–1892.
- (23) Li, Y.; Hao, J.; Liu, H.; Li, Y.; Ma, Y. The Metallization and Superconductivity of Dense Hydrogen Sulfide. *J. Chem. Phys.* **2014**, *140*, 174712.
- (24) Zeng, Q.; Yu, S.; Li, D.; Oganov, A. R.; Frapper, G. Emergence of Novel Hydrogen Chlorides under High Pressure. *Phys. Chem. Chem. Phys.* **2017**, *19*, 8236–8242.
- (25) Duan, D.; Tian, F.; Huang, X.; Li, D.; Yu, H.; Liu, Y.; Ma, Y.; Liu, B.; Cui, T. Decomposition of Solid Hydrogen Bromide at High Pressure. arXiv:1504.01196 2015. <https://arxiv.org/abs/1504.01196>.

- (26) Li, Y.; Gao, G.; Xie, Y.; Ma, Y.; Cui, T.; Zou, G. Superconductivity at ~ 100 K in Dense $\text{SiH}_4(\text{H}_2)_2$ Predicted by First Principles. *Proc. Natl. Acad. Sci. U. S. A.* **2010**, *107*, 15708.
- (27) Sun, Y.; Lv, J.; Xie, Y.; Liu, H.; Ma, Y. Route to a Superconducting Phase above Room Temperature in Electron-Doped Hydride Compounds under High Pressure. *Phys. Rev. Lett.* **2019**, *123*, No. 097001.
- (28) Peng, F.; Sun, Y.; Pickard, C. J.; Needs, R. J.; Wu, Q.; Ma, Y. Hydrogen Clathrate Structures in Rare Earth Hydrides at High Pressures: Possible Route to Room-Temperature Superconductivity. *Phys. Rev. Lett.* **2017**, *119*, 107001.
- (29) Salke, N. P.; Esfahani, M. M. D.; Zhang, Y.; Kruglov, I. A.; Zhou, J.; Wang, Y.; Greenberg, E.; Prakapenka, V. B.; Liu, J.; Oganov, A. R.; et al. Synthesis of Clathrate Cerium Superhydride CeH_9 at 80–100 GPa with Atomic Hydrogen Sublattice. *Nat. Commun.* **2019**, *10*, 4453.
- (30) Kruglov, I. A.; Kvashnin, A. G.; Goncharov, A. F.; Oganov, A. R.; Lobanov, S. S.; Holtgrewe, N.; Jiang, S.; Prakapenka, V. B.; Greenberg, E.; Yanilkin, A. V. Uranium Polyhydrides at Moderate Pressures: Prediction, Synthesis, and Expected Superconductivity. *Sci. Adv.* **2018**, *4*, eaat9776.
- (31) Semenok, D. V.; Kvashnin, A. G.; Kruglov, I. A.; Oganov, A. R. Actinium Hydrides AcH_{10} , AcH_{12} , and AcH_{16} as High-Temperature Conventional Superconductors. *J. Phys. Chem. Lett.* **2018**, *9*, 1920–1926.
- (32) Kvashnin, A. G.; Semenok, D. V.; Kruglov, I. A.; Wrona, I. A.; Oganov, A. R. High-Temperature Superconductivity in a Th-H System under Pressure Conditions. *ACS Appl. Mater. Interfaces* **2018**, *10*, 43809–43816.
- (33) Semenok, D. V.; Kvashnin, A. G.; Ivanova, A. G.; Svitlyk, V.; Fominiski, V. Y.; Sadakov, A. V.; Sobolevskiy, O. A.; Pudalov, V. M.; Troyan, I. A.; Oganov, A. R. Superconductivity at 161 K in Thorium Hydride ThH_{10} : Synthesis and Properties. *Mater. Today* **2020**, *33*, 36–44.
- (34) Zhou, D.; Semenok, D. V.; Duan, D.; Xie, H.; Chen, W.; Huang, X.; Li, X.; Liu, B.; Oganov, A. R.; Cui, T. Superconducting Praseodymium Superhydrides. *Sci. Adv.* **2020**, *6*, eaax6849.
- (35) Semenok, D. V.; Kruglov, I. A.; Savkin, I. A.; Kvashnin, A. G.; Oganov, A. R. On Distribution of Superconductivity in Metal Hydrides. *Curr. Opin. Solid State Mater. Sci.* **2020**, *24*, 100808.
- (36) Xiao, X.; Duan, D.; Xie, H.; Shao, Z.; Li, D.; Tian, F.; Song, H.; Yu, H.; Bao, K.; Cui, T. Structure and Superconductivity of Protactinium Hydrides under High Pressure. *J. Phys.: Condens. Matter* **2019**, *31*, 315403.
- (37) Cunningham, N. C.; Qiu, W.; Hope, K. M.; Liermann, H.-P.; Vohra, Y. K. Symmetry Lowering under High Pressure: Structural Evidence for *f*-Shell Delocalization in Heavy Rare Earth Metal Terbium. *Phys. Rev. B* **2007**, *76*, 212101.
- (38) Vaitheeswaran, G.; Kanchana, V.; Heathman, S.; Idiri, M.; Le Bihan, T.; Svane, A.; Delin, A.; Johansson, B. Elastic Constants and High-Pressure Structural Transitions in Lanthanum Monochalcogenides from Experiment and Theory. *Phys. Rev. B* **2007**, *75*, 184108.
- (39) Wang, Y.; Lv, J.; Zhu, L.; Ma, Y. Crystal Structure Prediction via Particle-Swarm Optimization. *Phys. Rev. B* **2010**, *82*, No. 094116.
- (40) Wang, Y.; Lv, J.; Zhu, L.; Ma, Y. CALYPSO: A Method for Crystal Structure Prediction. *Comput. Phys. Commun.* **2012**, *183*, 2063–2070.
- (41) Perdew, J. P.; Burke, K.; Ernzerhof, M. Generalized Gradient Approximation Made Simple. *Phys. Rev. Lett.* **1996**, *77*, 3865.
- (42) Kresse, G.; Joubert, D. From Ultrasoft Pseudopotentials to the Projector Augmented-Wave Method. *Phys. Rev. B* **1999**, *59*, 1758–1775.
- (43) Kresse, G.; Furthmüller, J. Efficiency of Ab-Initio Total Energy Calculations for Metals and Semiconductors Using a Plane-Wave Basis Set. *Comput. Mater. Sci.* **1996**, *6*, 15–50.
- (44) Kresse, G.; Furthmüller, J. Efficient Iterative Schemes for *Ab Initio* Total-Energy Calculations Using a Plane-Wave Basis Set. *Phys. Rev. B* **1996**, *54*, 11169–11186.
- (45) Giannozzi, P.; Baroni, S.; Bonini, N.; Calandra, M.; Car, R.; Cavazzoni, C.; Ceresoli, D.; Chiarotti, G. L.; Cococcioni, M.; Dabo, I.; et al. QUANTUM ESPRESSO: A Modular and Open-Source Software Project for Quantum Simulations of Materials. *J. Phys.: Condens. Matter* **2009**, *21*, 395502.
- (46) Giannozzi, P.; Andreussi, O.; Brumme, T.; Bunau, O.; Nardelli, M. B.; Calandra, M.; Car, R.; Cavazzoni, C.; Ceresoli, D.; Cococcioni, M.; et al. Advanced Capabilities for Materials Modelling with Quantum ESPRESSO. *J. Phys.: Condens. Matter* **2017**, *29*, 465901.
- (47) Baroni, S.; de Gironcoli, S.; Dal Corso, A.; Giannozzi, P. Phonons and Related crystal Properties from Density-Functional Perturbation Theory. *Rev. Mod. Phys.* **2001**, *73*, 515.
- (48) Cococcioni, M.; de Gironcoli, S. Linear response approach to the calculation of the effective interaction parameters in the LDA+U method. *Phys. Rev. B* **2005**, *71*, No. 035105.
- (49) Xie, H.; Yao, Y.; Feng, X.; Duan, D.; Song, H.; Zhang, Z.; Jiang, S.; Redfern, S. A. T.; Kresin, V. Z.; Pickard, C. J.; et al. Hydrogen Pentagraphenelike Structure Stabilized by Hafnium: A High-Temperature Conventional Superconductor. *Phys. Rev. Lett.* **2020**, *125*, 217001.
- (50) Mishra, A. K.; Muramatsu, T.; Liu, H.; Geballe, Z. M.; Somayazulu, M.; Ahart, M.; Baldini, M.; Meng, Y.; Zurek, E.; Hemley, R. J. New Calcium Hydrides with Mixed Atomic and Molecular Hydrogen. *J. Phys. Chem. C* **2018**, *122*, 19370–19378.
- (51) Ye, X.; Zarifi, N.; Zurek, E.; Hoffmann, R.; Ashcroft, N. W. High Hydrides of Scandium under Pressure: Potential Superconductors. *J. Phys. Chem. C* **2018**, *122*, 6298–6309.
- (52) Heil, C.; di Cataldo, S.; Bachelet, G. B.; Boeri, L. Superconductivity in Soda-Lite-Like Yttrium Hydride Clathrates. *Phys. Rev. B* **2019**, *99*, 220502.
- (53) Heyd, J.; Scuseria, G. E.; Ernzerhof, M. Erratum: “Hybrid Functionals Based on A Screened Coulomb Potential” [J. Chem. Phys. 118, 8207 (2003)]. *J. Chem. Phys.* **2006**, *124*, 219906.
- (54) Allen, P. B.; Dynes, R. C. Transition Temperature of Strong-Coupled Superconductors Reanalyzed. *Phys. Rev. B* **1975**, *12*, 905–922.
- (55) Zurek, E.; Bi, T. High-Temperature Superconductivity in Alkaline and Rare Earth Polyhydrides at High Pressure: A Theoretical Perspective. *J. Chem. Phys.* **2019**, *150*, No. 050901.